A&A, 684, L7 (2024)
https://doi.org/10.1051/0004-6361/202348452

Astronomy & Astrophysics

LETTER TO THE EDITOR

Tracking the motion of a shock along a channel in the low solar corona

J. Rigney[1,2,3], P. T. Gallagher[1], G. Ramsay[2], J. G. Doyle[2], D. M. Long[4,3], O. Stepanyuk[5], and K. Kozarev[5]

[1] Astronomy & Astrophysics Section, DIAS Dunsink Observatory, Dublin Institute for Advanced Studies, Dublin D15 XR2R, Ireland
e-mail: jeremy.rigney@dias.ie
[2] Armagh Observatory and Planetarium, College Hill, Armagh BT61 9DG, N. Ireland, UK
[3] School of Mathematics and Physics, Queen's University Belfast, University Road, Belfast BT7 1NN, N. Ireland, UK
[4] Centre for Astrophysics and Relativity, School of Physical Sciences, Dublin City University, Dublin D09 V209, Ireland
[5] Institute of Astronomy and National Astronomical Observatory, Bulgarian Academy of Sciences, Tsarigradsko Chausee Blvd 72, Sofia 1784, Bulgaria

Received 31 October 2023 / Accepted 21 March 2024

ABSTRACT

Context. Shock waves are excited by coronal mass ejections (CMEs) and large-scale extreme-ultraviolet (EUV) wave fronts and can result in low-frequency radio emission under certain coronal conditions.
Aims. In this work, we investigate a moving source of low-frequency radio emission as a CME and an associated EUV wave front move along a channel of a lower density, magnetic field, and Alfvén speed in the solar corona.
Methods. Observations from the Atmospheric Imaging Assembly on board the Solar Dynamics Observatory, the Nançay Radio Heliograph (NRH), and the Irish Low Frequency Array (I-LOFAR) were analysed. Differential emission measure maps were generated to determine densities and Alfvén maps, and the kinematics of the EUV wave front was tracked using CorPITA. The radio sources' positions and velocity were calculated from NRH images and I-LOFAR dynamic spectra.
Results. The EUV wave expanded radially with a uniform velocity of ~500 km s^{-1}. However, the radio source was observed to be deflected and appeared to move along a channel of a lower Alfvén speed, abruptly slowing from 1700 km s^{-1} to 250 km s^{-1} as it entered a quiet-Sun region. A shock wave with an apparent radial velocity of >420 km s^{-1} was determined from the drift rate of the associated Type II radio burst.
Conclusions. The apparent motion of the radio source may have resulted from a wave front moving along a coronal wave guide or by different points along the wave front emitting at locations with favourable conditions for shock formation.

Key words. Sun: corona – Sun: flares – Sun: radio radiation – Sun: UV radiation

1. Introduction

Observations of solar activity such as flares and coronal mass ejections (CMEs) can help us to better understand magnetic field dynamics, particle acceleration, and plasma motion. A more complete picture of these events can be obtained through multi-wavelength observations (cf. Warmuth et al. 2004; Raftery et al. 2009). Extreme-ultraviolet (EUV) observations from instruments, such as the Atmospheric Image Assembly (AIA; Lemen et al. 2012) on board the Solar Dynamics Observatory (SDO; Pesnell et al. 2012), image the upper chromosphere and corona, detecting events such as flares, CMEs, and EUV waves (Liu & Ofman 2014). EUV waves are defined as 'arc-shaped fronts' that propagate through the low corona from a shock origin and appear as the footprint of the outward propagating shock front (Gallagher & Long 2011; Long et al. 2011, 2017a). Measuring the velocity of EUV waves can give us insight into plasma conditions in the low solar corona and the dynamics of plasma motion in high-strength magnetic field environments (Gallagher et al. 2003; Long et al. 2013). While their origin is still disputed, a clear association has been made between the formation of EUV waves at the base of shocks (Thompson et al. 1998; Long et al. 2019). EUV waves are also known to undergo reflection and refraction at coronal hole boundaries, regions of distinct change in the plasma density, and magnetic field environments (Gopalswamy et al. 2009).

Low-frequency solar radio emission (<1 GHz) is emitted by accelerated electrons in the corona (Wild 1950). Type II radio bursts are formed when accelerated plasma surpasses the local Alfvén speed in the surrounding undisturbed environment to form a shock (Nelson & Melrose 1985). These super-Alfvénic shocks typically occur higher in the solar corona in lower-density plasma environments where the Alfvén speed is lower. In dynamic spectra, Type II bursts are characterised by fundamental and harmonic bands that drift from high to low frequency over time, corresponding to the changing plasma frequency at different heights in the corona. Fine structures within these bands reveal electron acceleration and conditions within the shock (Magdalenić et al. 2020). Solar radio imaging during these events can also help determine the propagation of the shock front and regions of electron acceleration. Instruments such as the LOw Frequency ARray (LOFAR; van Haarlem et al. 2013) and the Nançay Radio Heliograph (NRH; Kerdraon & Delouis 2007) are capable of providing high-resolution imaging and dynamic spectra of the Sun via dedicated monitoring programmes.

The relationship between Type II radio bursts and EUV waves has been studied extensively (Vršnak et al. 2005; Magdalenić et al. 2008; Kouloumvakos et al. 2014; Morosan et al. 2019). Prior to the first observation of global EUV waves in 1997 (Dere et al. 1997; Thompson et al. 1998), Type II radio bursts were thought to be produced by the same physical process driving Moreton-Ramsey waves (first observed by Moreton 1960; Moreton & Ramsey 1960). However, the significant discrepancy in velocity between Moreton-Ramsey and EUV waves complicated this assumption (see, e.g. the reviews of EUV wave observations by Gallagher & Long 2011; Warmuth 2015), leading to a series of statistical studies examining their relationship. Initially, Klassen et al. (2000) found that 90% of Type II radio bursts observed in 1997 were associated with global EUV waves. However, subsequent work by Biesecker et al. (2002) found that only 29% of the EUV waves in the catalogue compiled from SOHO/EIT observations by Thompson & Myers (2009) had associated Type II radio bursts. Muhr et al. (2014) obtained comparable results, finding that 22% of 60 EUV waves observed using the higher-resolution imaging provided by STEREO/EUVI had an associated Type II radio burst. The advent of very high-resolution observations from SDO/AIA enabled Nitta et al. (2013) to assemble and examine a catalogue of 138 global EUV waves, finding that 54% were associated with Type II radio bursts. However, using the catalogue of Nitta et al. (2013) as a starting point, Long et al. (2017b) found no clear relationship between global EUV waves identified using the automated Coronal Pulse Identification and Tracking Algorithm (CorPITA; Long et al. 2014) and Type II radio bursts. The relationship between these phenomena therefore continues to be a source of much investigation, with Fulara & Kwon (2021) suggesting that Type II bursts are more related to the velocity of the erupting CME than the laterally propagating global EUV wave.

Most observations capture events on or near the limb, as the height and outward propagation of radio emission can be more accurately determined. Previous research with similar observations of EUV waves and Type II radio bursts have, for the most part, concluded that these events are linked via shock formation from flares and CMEs (see Grechnev et al. 2012). While much of the previous research has examined the links between EUV waves and radio emission, it is difficult to capture high-cadence multi-wavelength (X-ray, EUV, and radio) observations for a single event containing a high-energy flare, shock, and EUV wave. Furthermore, on-disk events can be difficult to characterise but are important for space weather as rapid on-disk events can release sudden energetic particle (SEP) events towards Earth (e.g. Desai & Giacalone 2016).

In this Letter observations of an impulsive X-class flare from 10 May 2022 were presented, where both a shock front and EUV wave were observed by SDO and the Geostationary Operational Environmental Satellite (GOES), Irish LOw Frequency ARray (I-LOFAR Murphy et al. 2021), the Observations Radio pour Fedome et l'Etude des Eruptions Solaires radio-spectrograph (ORFEES; Hamini et al. 2021), and the NRH. We summarise the characteristics of the radio emission, the propagation of the EUV wave, and the relation between both phenomena. Observations are reported in Sect. 2. An analysis of the data and results are in Sect. 3, and a brief discussion and conclusions are provided in Sect. 4.

2. Observations

On 10 May 2022 at 13:50 UT, an X 1.5 class solar flare occurred originating from active region NOAA AR13006. The solar flare was accompanied by a shock event. This event began less than 10 min after a C-class flare from the eastern limb of the Sun.

2.1. Radio dynamic spectrum

I-LOFAR was conducting solar observations on 10 May 2022 with data recorded by the REAL-time Transient Acquisition (REALTA) system (Murphy et al. 2021). The I-LOFAR station forms part of the International LOFAR Telescope (van Haarlem et al. 2013) and observes with low band antennas at 10–90 MHz, and high band antennas from 110–230 MHz. The telescope can be configured to observe a target with both antenna sets, utilising the full frequency band of 10–240 MHz. Using the REALTA pipeline allows observations to be recorded at 5.12 µs time resolution, and 195 kHz frequency resolution. The data for this project were stored at a down-sampled time resolution of 1.2 ms. I-LOFAR captured a dynamic spectrum with a number of Type III bursts prior to the X-ray flare observed by GOES. A Type II radio burst was recorded 3 min after the peak of the X-ray emission, lasting for approximately 15 min (see Fig. 1). The Type II burst displayed a band split in both the fundamental and harmonic bands, as seen in previous work by Maguire et al. (2020) and Magdalenić et al. (2020).

ORFEES was also observing the Sun during the X-class event at a cadence of 0.1 s and a frequency range of 144–1000 MHz. At the peak of the flare (13:57 UT), a high-frequency Type III radio burst was detected between 300–800 MHz.

During the Type II burst observed by I-LOFAR, a Type IV burst also occurred at frequencies ranging from ∼100 to ∼500 MHz. This diffuse broadband radio emission was observed by all three radio instruments, I-LOFAR, ORFEES, and NRH.

2.2. AIA EUV imaging

The on–disk signatures of the global EUV wave were identified using observations from the AIA on board SDO. The global EUV wave could be visually identified and compared to the position of the radio emission using three–colour running ratio images (as shown in Fig. 1; see Downs et al. 2012, for more details). As can be seen in Fig. 1, the wave front was highly directional, mainly propagating to the north-east of the erupting active region, with some indication of wave-front propagation to the south of the active region, similar to the observed radio emission. The kinematics of the global wave front were estimated using the arc-sector approach of Long et al. (2014) to enable a direct comparison with the kinematics of the observed radio emission. A series of arc sectors of 10° width were applied to the 12 s cadence data from the AIA 211 Å pass band to produce distance-time plots that showed the temporal evolution of the wave front along each arc sector. The leading edge of the wave front could then be manually identified as previously described by Long et al. (2021) and compared to the observed radio signature.

2.3. Radio imaging

Radio images sampled at 0.25 s cadence at 154 MHz and 408 MHz were obtained from NRH (Fig. 1b). This provided spatial information for the location of the radio emission that is accurate to 10″ at 154 MHz. The location of the peak radio flux was measured for each image, and the motion of the radio source was recorded for comparison to the EUV wave propagation. The NRH radio images were used for timing analysis to confirm that the Type II radio burst captured with I-LOFAR originated from the flaring active region.

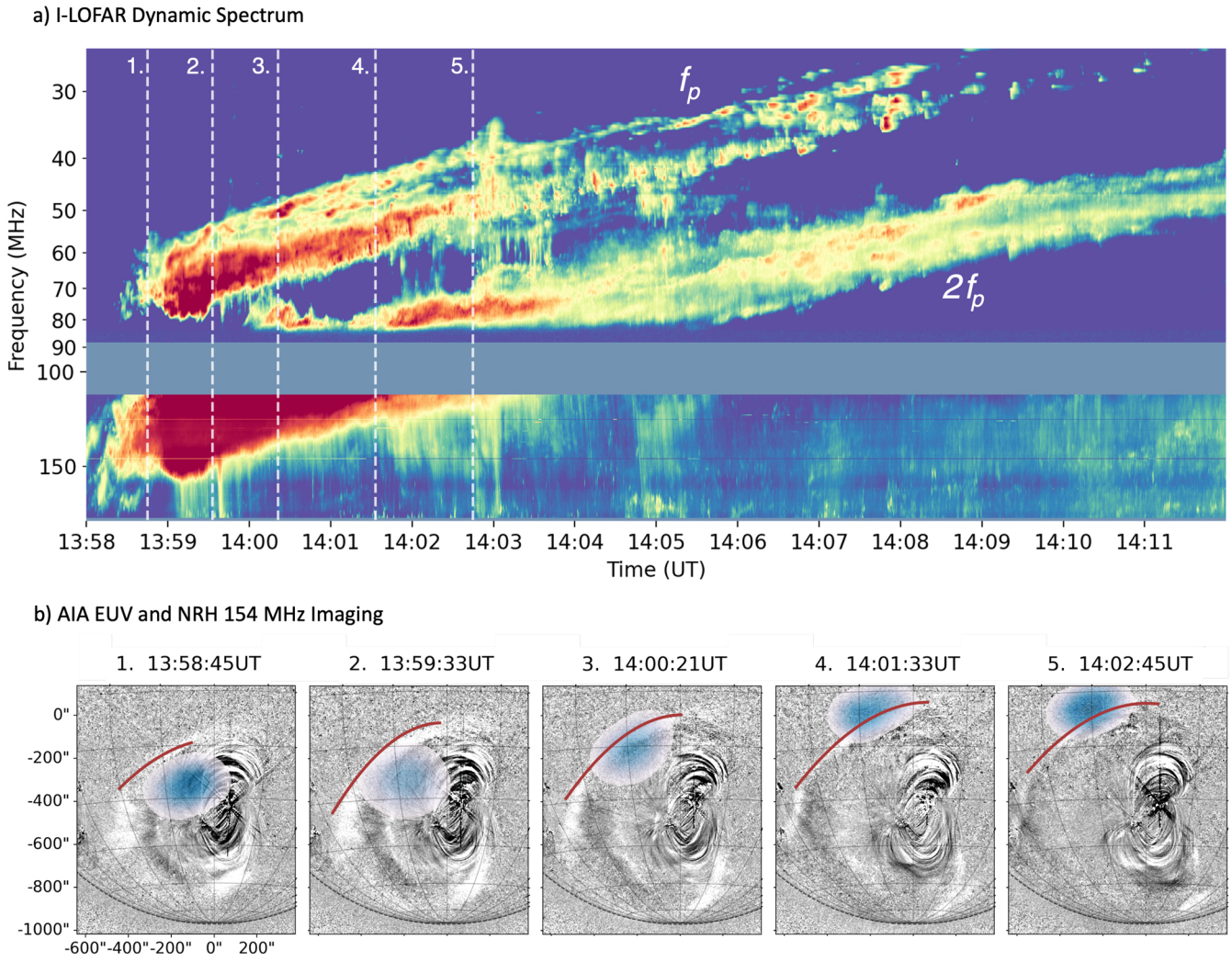

Fig. 1. Summary of 10 May 2022 event captured by three instruments. (a): I–LOFAR dynamic spectrum of the Type II radio burst, highlighting the bright fundamental and harmonic bands. The fundamental band drifts from ~60 MHz to ~25 MHz over 15 min, with band-splitting occurring within both the fundamental and harmonic lanes. Dashed vertical lines correspond to the timestamps of images in the lower panel. (b): AIA three-channel difference imaging. Overlaid in blue in each panel is the 3σ–to–peak NRH 154 MHz radio source. The solid red line is the EUV wave front that was identified from the CorPITA difference imaging.

Two clear 154 MHz radio sources on the solar disk were observed propagating away from the active region for a short time after the flare. The southward propagating radio emission quickly faded after approximately 40 s. The northward propagating radio emission was observed for approximately 7 min, with clear motion of the peak along the axis of propagation of the EUV wave. The motion of the 154 MHz peak was measured to determine the velocity across the solar disk.

The radio imaging also revealed that a Type III noise storm observed prior to the X-class flare. The source originated from AR3007 on the eastern limb where an earlier C-class flare originated and was not related to the X-class event.

3. Data analysis and results

3.1. Dynamic spectrum

Background subtraction was performed on the dynamic spectrum to flatten the frequency response of the LOFAR antennas. The Type II burst within the spectrum displayed a number of fine structures resolvable at high time resolution. The fundamental (start: 60 MHz, f_p) and harmonic (start: 120 MHz, $2f_p$) bands are observed with a clear separation in Fig. 1a. Within these bands, herringbone structures are visible (Carley et al. 2013; Morosan et al. 2019). The fundamental band displays band-splitting. Using the same method as described in Vršnak et al. (2002) and Maguire et al. (2020), an estimate of the Alfvén Mach number was made for the duration of the Type II burst from the separation of the band-splitting. The Alfvén Mach number ranged between 1.5 and 1.6 throughout the shock. This burst had a drift rate of 0.59 MHz s^{-1}.

Points were selected along the leading edge of the Type II burst fundamental band at regular time intervals. The Mann solar density model (Mann & Klassen 2005) was used to calculate the shock speed from the leading edge of the Type II burst. Other electron density models were also investigated, including densities typical of both coronal hole and quiet-Sun conditions (Newkirk 1961; Doyle et al. 1999); however, the event studied here occurred near an active region so these were not suitable. A mean shock velocity of 420^{+150}_{-120} km s^{-1} was determined using this method (see Fig. 1).

Other fine structures were observed within the event, including flag, spike, and sail-like features consistent with those observed in Magdalenić et al. (2020). An interesting phenomenon observed at the end of the Type II burst (approx. 14:15 UT) is the appearance of two further lanes or bands that mirror the end of the Type II burst but at a later time. These later bands also appear to display band-splitting but their source is unknown.

A Type IV radio burst was recorded after the Type II burst, ranging in frequencies from 20–500 MHz. The Type IV burst had fine vertical structures resembling herringbone structures.

3.2. EUV wave velocity

The velocity of the EUV wave front was measured accounting for the propagation across the solar disk. Two methods were used to estimate this velocity, CorPITA (Long et al. 2014) and Wavetrack, (Stepanyuk et al. 2022). Figure 1b contains the morphology of the EUV wave front for the duration of the event. The area surrounding the active region was divided into 10° segments. A velocity profile for each segment was created using wave-front detection with CorPITA. Segments with angles of propagation matching the 154 MHz radio emission were then examined in greater detail to determine the acceleration and dispersion profiles. The EUV wave velocity was measured for the region spatially overlapping the 154 MHz radio emission. The mean velocity of the wave during this time was ~500 km s^{-1}.

A second method was also employed to estimate the EUV wave velocity, using Wavetrack[1], a wavelet decomposition technique for wave-front detection and analysis. The Wavetrack object masks were applied to the running difference, using the AIA 193 Å observations. The Wavetrack was able to capture the extent of the wave in the consecutive time steps very well. To study the kinematics of the coronal front features in detail based on the Wavetrack output, the Fourier local correlation tracking (FLCT) method was employed (Welsch et al. 2004; Fisher & Welsch 2008), followed by centre of the mass velocity calculation. FLCT calculations show velocities of ~700 km s^{-1}, which is at the upper end of the error for the more commonly used CorPITA method.

3.3. Radio imaging

NRH images at 154 MHz and 408 MHz were examined to determine the emission propagation characteristics. *SolarSoft* (Freeland & Handy 1998) was used to produce images from the Nançay observations using the default pipeline settings. The location of the peak radio emission from the 154 MHz NRH imaging on the solar disk was recorded for each 0.25 s timestamp. The peak emission was observed to drift upwards across the solar disk contemporaneously with the propagation of the EUV wave in the low solar corona (Fig. 2). In order to determine if a correlation existed between the motion of the two events, the movement of the peak radio emission was recorded across the Sun. The 154 MHz band displayed rapidly moving north- and southward peaks. Two distinct velocity profiles can be seen in Fig. 3 initially travelling at ~1750 km s^{-1} in Phase 1, then slowing to ~230 km s^{-1} in Phase 2. The abrupt change in speed corresponds to the change in direction of the radio emission source from 14:01:55 UT, as highlighted in Fig. 2. The change in velocity of the radio source corresponds to the shock entering a region of lower density and Alfvén speed. This motion is also observed in Fig. 1 where the radio source appears to overtake the EUV wave front. Some uncertainty remains in the radio velocity estimates due to projection effects observing emission on-disk and radio source height estimates of 1.2 $R_\odot$ for the 154 MHz emission.

Magnetic field values were calculated using a potential field source surface (PFSS) extrapolation at 1.2 $R_\odot$ from Global Oscillation Network Group (GONG) magnetograms. Densities were determined from differential emission measure (DEM) maps (see Stansby et al. 2020) and `demregpy`[2]. The DEM map was integrated across all AIA temperature ranges $5.6 \leq \log_{10} T \leq 6.8$ K to produce a line-of-sight DEM. Regarding the DEM initial conditions, full details on the inversion method, in addition to assumptions relating errors and temperature resolution can be found in Hannah & Kontar (2012) where these authors tested the code on both simulated and real Hinode/EIS and SDA/AIA data. A height of 1.2 $R_\odot$ was used to determine the magnetic field values using the Mann density model. These values could then be used to create an Alfvén speed map of the region through which the radio source travelled. The Alfvén speed dropped from ~550 km s^{-1} near the active region to ~300 km s^{-1} in the quiet-Sun region. The cumulative distance versus time plot in Fig. 3 highlights the rapid onset acceleration and gradual decay in velocity as the radio source propagates upwards across the solar disk.

Stationary radio emission was observed at 408 MHz for the duration of the flare and CME event directly over the active region, and it occurred for the same duration and frequency range within the I-LOFAR dynamic spectrum as the Type IV radio burst.

3.4. Coronal channel

The 154 MHz radio source tracking the EUV wave was observed to deviate from a great circle path significantly. When compared to the Alfvén map, the radio source appears to rapidly move away from the higher Alfvén speed of the active region into a region of lower Alfvén speed. A physical explanation for this observed path could be the presence of a wave guide that formed by the surrounding conditions in the corona, creating a region favourable for electron acceleration in the propagating shock front. Understanding the complete picture of shock formation and evolution during the event is difficult due to the complex magnetic environment surrounding the active region. However, the EUV wave and radio emission propagate into a region of lower magnetic field strength, while the electron density does not vary dramatically. A high Alfvén speed suggests a shock wave is being formed for the majority of the duration of the event.

The EUV wave front is not noticeably impacted by the coronal channel. It is possible that conditions conducive to radio emission in the upper corona are generated at different points along the shock front during the propagation. This would suggest that the observed radio emission is occurring where the shock is propagating quasi-perpendicular to the local magnetic field, generating the observed apparent non-uniform propagation. A similar phenomenon was observed in Koukras et al. (2020). Furthermore, electron density variations, while estimated with DEMs, are difficult to constrain at high spatial resolution at different heights in the corona. It is therefore also possible that the radio emission is occurring at different heights along the expanding shock front, further complicating the calculation of

[1] https://gitlab.com/iahelio/mosaiics/wavetrack

[2] https://github.com/alasdairwilson/demregpy

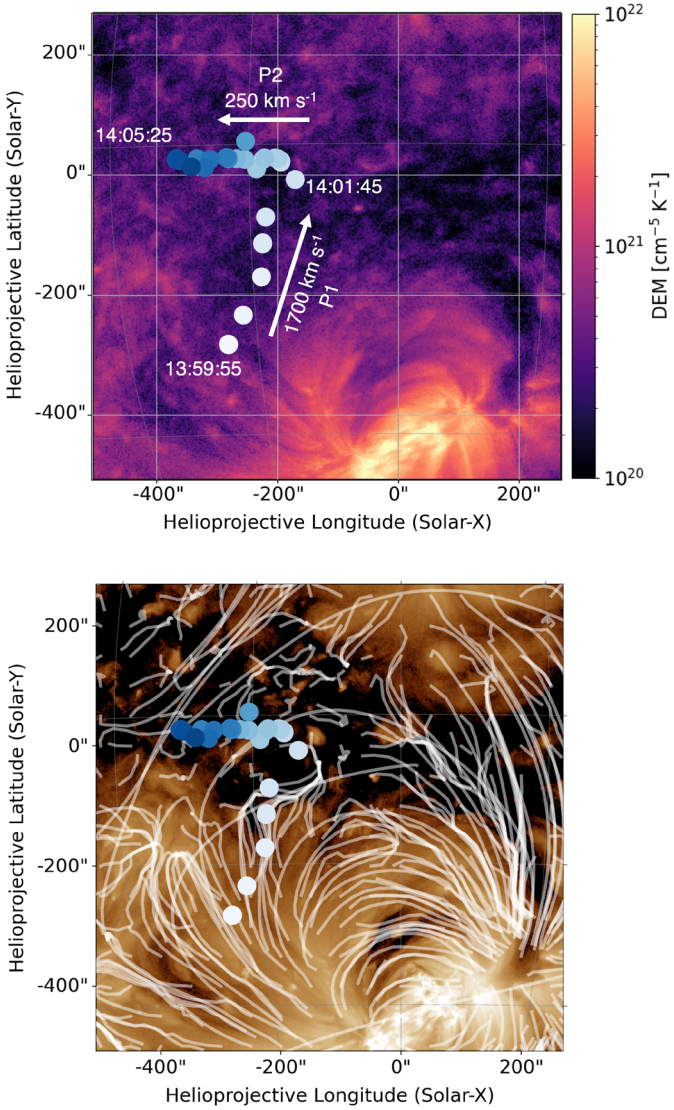

Fig. 2. Path of the 154 MHz radio source. (a): Line-of-sight-integrated DEM map. The white-to-blue points show the time evolution of the 154 MHz radio source in 10 s intervals. The velocities of the points in Phase 1 and Phase 2, obtained from 0.25 s data, are indicated by the labelled arrows. (b): Combination of an AIA 193 Å image during the event with a PFSS extrapolation. The radio emission clearly moves around a higher Alfvén speed region, favouring lower magnetic field strength regions.

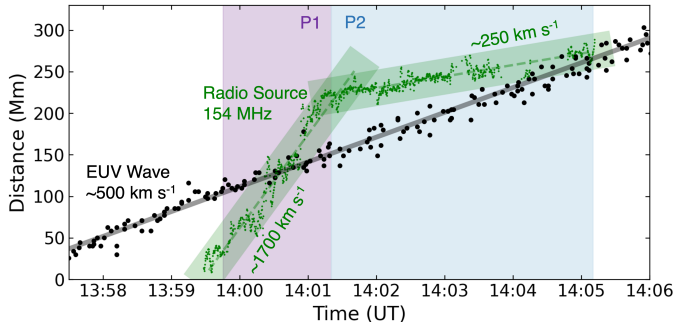

Fig. 3. Distance-time plot for CorPITA EUV wave (black points) and 0.25 s time resolution radio source (green points) with errors for each highlighted by shaded regions. The purple region (P1) highlights the region when the radio source initially travelled at a higher velocity, later slowing in the blue-shaded region (P2) once it reached the region of lower density. These correspond to the same emission marked in Fig. 2. The velocity of the EUV wave was 500 km s^{-1} and the radio source velocities were 1700 km s^{-1} and 250 km s^{-1}.

the velocity and path taken. Examining the direction of the magnetic field was beyond the scope of this research.

4. Discussion and conclusions

Multi-wavelength solar observations with NRH, AIA, and I-LOFAR on 10 May 2022 revealed an EUV wave and radio emission associated with an X-class flare and shock wave. Analysis of the observations from each instrument appears to show a spatial and temporal correlation between the EUV wave and radio emission imaged at the shock front. The EUV wave had a constant velocity of (~500 km s^{-1}). The associated 154 MHz radio source was measured to have an initial horizontal velocity of 1700 km s^{-1}, changing to 250 km s^{-1}. Using the Mann density model, a radial velocity of ~420 km s^{-1} was derived from the Type II burst, lying within the range of the EUV wave velocity. Our observations allowed us to examine shock propagation at different heights throughout the solar corona as the shock propagated across the solar disk.

This event was captured during the initial formation, propagation, and expansion of a coronal shock front. This may explain the lack of correlation between the EUV wave and 154 MHz radio imaging prior to 14:00 UT, as the shock was not self-similar in the initial expansion stage (Subramanian et al. 2014; Uralov et al. 2019). The event can be compared with emission observed from an off-limb event in 2005 in which an EUV wave, Type II radio burst, and low-frequency NRH imaging were observed from a CME event (Vršnak et al. 2005). The EUV wave was observed to slow and disperse into a region of lower density; this has been observed during previous events and predicted in simulations (Wu et al. 2001; Veronig et al. 2006).

The most probable scenario arising from all emission moving at similar velocities is that the emission source is linked. In this case the observed propagation outwards from the active region that produced the X-class flare suggests a shock wave that accelerated electrons in the upper corona, producing radio emission, while exciting plasma in the low corona at the base of the shock forming an EUV wave. The physical mechanism producing the 154 MHz radio emission and dynamic spectrum is most likely shock-accelerated electrons (plasma emission). The faint, weak EUV wave indicates low levels of disruption to the low solar corona, which propagates across the disk below the radio emission. Models of these events indicate regions where radio emission is expected to be produced in regions where the shock is propagating normally to the local magnetic fields (Zucca et al. 2014; Morosan et al. 2019).

Finally, we observed the motion of radio emission travelling along a coronal channel, bounded by regions of higher magnetic field strength. Phenomena such as EUV wave reflection and refraction support the case that shocks can be diverted and directed by conditions in the low corona. Two possible phenomena are occurring during this event, as interpreted from the motion of the 154 MHz radio emission. Either the shock is being guided through the channel of lower density, or the radio source is visible at points where the shock is quasi-perpendicular to the local magnetic field. The tracking of the motion of low-frequency radio emission also suggests that this guiding behaviour can occur at higher regions of the outer corona. Future analysis of similar events could probe the local

motion of an EUV wave in conditions where shock propagation travels through channels of lower magnetic field strengths, as well as search for a similar motion at different radio frequencies at different heights of a shock in the corona.

Acknowledgements. I-LOFAR receives funding from Science Foundation Ireland (SFI), the Department of Further and Higher Education, Research, Innovation and Science (DFHERIS) and the Department for Communities of the N. Ireland Executive via AOP. REALTA was funded by SFI and Breakthrough Listen. JGD would like to thank the Leverhulme Trust for an Emeritus Fellowship. DML is grateful to the Science Technology and Facilities Council for the award of an Ernest Rutherford Fellowship (ST/R003246/1). This work is partly supported by the European Union's Horizon 2020 research and innovation program under grant agreement 952439, project STELLAR (Scientific and Technological Excellence by Leveraging LOFAR Advancements in Radio Astronomy). K.K. and O.S. acknowledge support from the Bulgarian National Science Fund, VIHREN program, under contract KP-06-DV-8/18.12.2019.

References

Biesecker, D. A., Myers, D. C., Thompson, B. J., Hammer, D. M., & Vourlidas, A. 2002, ApJ, 569, 1009
Carley, E. P., Long, D. M., Byrne, J. P., et al. 2013, Nat. Phys., 9, 811
Dere, K. P., Brueckner, G. E., Howard, R. A., et al. 1997, Sol. Phys., 175, 601
Desai, M., & Giacalone, J. 2016, Liv. Rev. Sol. Phys., 13, 3
Downs, C., Roussev, I. I., van der Holst, B., Lugaz, N., & Sokolov, I. V. 2012, ApJ, 750, 134
Doyle, J., Teriaca, L., & Banerjee, D. 1999, A&A, 349, 956
Fisher, G. H., & Welsch, B. T. 2008, Subsurface and Atmospheric Influences on Solar Activity, 383, 373
Freeland, S., & Handy, B. 1998, Sol. Phys., 182, 497
Fulara, A., & Kwon, R.-Y. 2021, ApJ, 919, L7
Gallagher, P. T., & Long, D. M. 2011, Space Sci. Rev., 158, 365
Gallagher, P. T., Lawrence, G. R., & Dennis, B. R. 2003, ApJ, 588, 53
Gopalswamy, N., Yashiro, S., Temmer, M., et al. 2009, ApJ, 691, L123
Grechnev, V., Uralov, A., Chertok, I., et al. 2012, Energy Storage and Release through the Solar Activity Cycle: Models Meet Radio Observations (Springer), 127
Hamini, A., Auxepaules, G., Birée, L., et al. 2021, J. Space Weather Space Clim., 11, 57
Hannah, I. G., & Kontar, E. P. 2012, A&A, 539, A146
Kerdraon, A., & Delouis, J. M. 2007, Coronal Physics from Radio and Space Observations: Proceedings of the CESRA Workshop Held in Nouan le Fuzelier, France, 3-7 June 1996 (Springer), 192
Klassen, A., Aurass, H., Mann, G., & Thompson, B. 2000, A&AS, 141, 357
Koukras, A., Marqué, C., Downs, C., & Dolla, L. 2020, A&A, 644, A90
Kouloumvakos, A., Patsourakos, S., Hillaris, A., et al. 2014, Sol. Phys., 289, 2123
Lemen, J. R., Title, A. M., Akin, D. J., et al. 2012, Sol. Phys., 275, 17
Liu, W., & Ofman, L. 2014, Sol. Phys., 289, 3233
Long, D. M., Deluca, E. E., & Gallagher, P. T. 2011, ApJ, 741, 21
Long, D. M., Williams, D. R., Régnier, S., & Harra, L. K. 2013, Sol. Phys., 288, 567
Long, D. M., Bloomfield, D. S., Gallagher, P. T., & Pérez-Suárez, D. 2014, Sol. Phys., 289, 3279
Long, D. M., Bloomfield, D. S., Chen, P. F., et al. 2017a, Sol. Phys., 292, 7
Long, D. M., Murphy, P., Graham, G., Carley, E. P., & Pérez-Suárez, D. 2017b, Sol. Phys., 292
Long, D. M., Jenkins, J., & Valori, G. 2019, ApJ, 882, 90
Long, D. M., Reid, H. A. S., Valori, G., & O'Kane, J. 2021, ApJ, 921, 61
Magdalenić, J., Vršnak, B., Pohjolainen, S., et al. 2008, Sol. Phys., 253, 305
Magdalenić, J., Marqué, C., Fallows, R. A., et al. 2020, ApJ, 897, 15
Maguire, C. A., Carley, E. P., McCauley, J., & Gallagher, P. T. 2020, A&A, 633, A56
Mann, G., & Klassen, A. 2005, A&A, 441, 319
Moreton, G. E. 1960, AJ, 65, 494
Moreton, G. E., & Ramsey, H. E. 1960, PASP, 72, 357
Morosan, D. E., Carley, E. P., Hayes, L. A., et al. 2019, Nat. Astron., 3, 452
Muhr, N., Veronig, A. M., Kienreich, I. W., et al. 2014, Sol. Phys., 289, 4563
Murphy, P. C., Callanan, P., Mccauley, J., et al. 2021, A&A, 655, A16
Nelson, G., & Melrose, D. 1985, Solar Radiophysics: Studies of Emission from the Sun at Metre Wavelengths (New York: Cambridge University Press), 333
Newkirk, G., Jr 1961, ApJ, 133, 983
Nitta, N. V., Schrijver, C. J., Title, A. M., & Liu, W. 2013, ApJ, 776, 58
Pesnell, W. D., Thompson, B. J., & Chamberlin, P. C. 2012, Sol. Phys., 275, 3
Raftery, C. L., Gallagher, P. T., Milligan, R. O., & Klimchuk, J. A. 2009, A&A, 494, 1127
Stansby, D., Yeates, A., & Badman, S. T. 2020, J. Open Source Software, 5, 2732
Stepanyuk, O., Kozarev, K., & Nedal, M. 2022, J. Space Weather Space Clim., 12, 20
Subramanian, P., Arunbabu, K., Vourlidas, A., & Mauriya, A. 2014, ApJ, 790, 125
Thompson, B. J., & Myers, D. C. 2009, ApJS, 183, 225
Thompson, B. J., Plunkett, S. P., Gurman, J. B., et al. 1998, Geophys. Res. Lett., 25, 2465
Uralov, A., Grechnev, V., & Ivanukin, L. 2019, Sol. Phys., 294, 1
van Haarlem, M. P., Wise, M. W., Gunst, A., et al. 2013, A&A, 556, A2
Veronig, A. M., Temmer, M., Vršnak, B., & Thalmann, J. K. 2006, ApJ, 647, 1466
Vršnak, B., Magdalenić, J., Aurass, H., & Mann, G. 2002, A&A, 396, 673
Vršnak, B., Magdalenić, J., Temmer, M., et al. 2005, ApJ, 625, L67
Warmuth, A. 2015, Liv. Rev. Sol. Phys., 12, 3
Warmuth, A., Vršnak, B., Magdalenić, J., Hanslmeier, A., & Otruba, W. 2004, A&A, 418, 1101
Welsch, B., Fisher, G., Abbett, W., & Regnier, S. 2004, ApJ, 610, 1148
Wild, J. 1950, Aust. J. Chem., 3, 399
Wu, S., Zheng, H., Wang, S., et al. 2001, J. Geophys. Res.: Space Phys., 106, 25089
Zucca, P., Carley, E. P., Bloomfield, D. S., & Gallagher, P. T. 2014, A&A, 564, A47